Publications

11-12-2020

The Dynamics of Nonlinear Atmospheric Acoustic-Gravity Waves Generated by Tsunamis Over Realistic Bathymetry

P. A. Inchin
Embry-Riddle Aeronautical University, INCHINP@my.erau.edu

C. J. Heale
Embry-Riddle Aeronautical University, HEALEC@erau.edu

J. B. Snively
Embry-Riddle Aeronautical University, snivelyj@erau.edu

M. D. Zettergren
Embry-Riddle Aeronautical University, zettergm@erau.edu

Follow this and additional works at: https://commons.erau.edu/publication

Part of the Geophysics and Seismology Commons

Scholarly Commons Citation

Correspondence to:
P. A. Inchin,
inchinp@erau.edu

The Dynamics of Nonlinear Atmospheric Acoustic-Gravity Waves Generated by Tsunamis Over Realistic Bathymetry

P. A. Inchin[1] , **C. J. Heale[1]** , **J. B. Snively[1]** , and **M. D. Zettergren[1]**

[1]Department of Physical Sciences and Center for Space and Atmospheric Research, Embry-Riddle Aeronautical University, Daytona Beach, FL, USA

Abstract The investigation of atmospheric tsunamigenic acoustic and gravity wave (TAGW) dynamics, from the ocean surface to the thermosphere, is performed through the numerical computations of the 3D compressible nonlinear Navier-Stokes equations. Tsunami propagation is first simulated using a nonlinear shallow water model, which incorporates instantaneous or temporal evolutions of initial tsunami distributions (ITD). Ocean surface dynamics are then imposed as a boundary condition to excite TAGWs into the atmosphere from the ground level. We perform a case study of a large tsunami associated with the 2011 M9.1 Tohuku-Oki earthquake and parametric studies with simplified and demonstrative bathymetry and ITD. Our results demonstrate that TAGW propagation, controlled by the atmospheric state, can evolve nonlinearly and lead to wave self-acceleration effects and instabilities, followed by the excitation of secondary acoustic and gravity waves (SAGWs), spanning a broad frequency range. The variations of the ocean depth result in a change of tsunami characteristics and subsequent tilt of the TAGW packet, as the wave's intrinsic frequency spectrum is varied. In addition, focusing of tsunamis and their interactions with seamounts and islands may result in localized enhancements of TAGWs, which further indicates the crucial role of bathymetry variations. Along with SAGWs, leading long-period phases of the TAGW packet propagate ahead of the tsunami wavefront and thus can be observed prior to the tsunami arrival. Our modeling results suggest that TAGWs from large tsunamis can drive detectable and quantifiable perturbations in the upper atmosphere under a wide range of scenarios and uncover new challenges and opportunities for their observations.

1. Introduction

Ocean surface gravity waves (tsunamis) are a well-known sources of waves in the atmosphere, as fluid quantities on water-air interface must be conserved (Davies & Baker, 1965; Godin et al., 2015; Peltier & Hines, 1976). Exponential decrease of neutral atmospheric mass density with altitude leads to the substantial amplification of tsunamigenic acoustic and gravity waves (collectively, TAGWs), with periods from tens of seconds to tens of minutes. Today, a broad range of ground- and space-based instruments provide unprecedented opportunities for the investigation of TAGW dynamics through the observations of neutral and charged particle disturbances caused by them (Coïsson et al., 2015; Galvan et al., 2011; Yang et al., 2017). Collected data enable new scientific investigations of natural hazard-atmosphere-ionosphere coupled processes and can motivate important future applications in detections or diagnostics (Kamogawa et al., 2016; Rakoto et al., 2018; Savastano et al., 2017).

Undersea earthquakes generate the majority of large tsunamis (Levin & Nosov, 2016), and main features of TAGWs excited by them have been widely investigated (e.g., Artru et al., 2005; Hickey et al., 2009; Huba et al., 2015; Occhipinti et al., 2013; Vadas et al., 2015). As with other acoustic-gravity waves (AGWs), the propagation of TAGWs is controlled by the atmospheric state, which may result in their reflection, refraction, and tilting (Broutman et al., 2014; Heale & Snively, 2015; Wu et al., 2016), tunneling (Sutherland & Yewchuk, 2004; Yu & Hickey, 2007), ducting (Chimonas & Hines, 1986; Snively & Pasko, 2008), and damping and interference (Sutherland, 2006; Vadas, 2007). Nonlinear effects, breaking, self-acceleration and dissipation are of particular importance for their propagation in the upper atmosphere (Fritts et al., 2015; Heale et al., 2014; Walterscheid & Schubert, 1990). However, there remains a lack of comprehensive modeling studies, which incorporate realistically varying tsunami waves coupled with compressible and nonlinear

models, thus spanning from the ocean to the upper atmosphere. Models lacking comprehensive physics may suggest marked underestimation or overestimation of TAGW amplitudes due to insufficient accounting for nonlinearity, that would otherwise lead to evolution of their spectra or dissipation. It is fair to assume that temporal and spatial evolution of ocean surface waves, their interaction with bathymetry, and shores, interference, dispersion, and nonlinear effects should also affect TAGW characteristics, and to the best of our knowledge, this was not yet addressed in a literature.

Here, we report simulation results of TAGW dynamics based on the 2011 Japan Tohoku-Oki tsunami case study, incorporating tsunami evolution over realistic bathymetry. Tsunami simulation is performed in a nonlinear shallow-water model. The results of a forward seismic wave propagation simulation are used as a temporally varying initial tsunami distribution (ITD). TAGW excitation and propagation from the ocean to 500 km height are simulated in 3D compressible nonlinear neutral atmosphere model. Separately, we investigate source and bathymetry effects on TAGWs through parametric 2D and 3D simulations with simplified and demonstrative ITDs and ocean seafloor variations.

Our results demonstrate that TAGW propagation is affected by the atmospheric state and nonlinear evolution, as well known for other short-period gravity waves (Fritts et al., 2015). Substantial amplitudes of TAGWs in the thermosphere can lead to instabilities, followed by the excitation of secondary acoustic and gravity waves (SAGWs), spanning a broad range of periods (e.g., Bossert et al., 2017; Heale et al., 2020, and references therein). Bathymetry plays a crucial role on TAGW characteristics. Particularly, ocean depth changes result in TAGW amplitude increase or decrease at different altitudes, as the whole TAGW packet tilts from the variations of the intrinsic frequencies of excited in the atmosphere TAGWs, exhibiting different dissipation altitudes. Focusing of tsunami waves over rises and their interaction with seamounts and islands can lead to the substantial enhancement of the generated TAGWs. Long-period TAGWs that propagate ahead of the tsunami wavefront may generate early-detectable perturbations, whereas the dissipation of primary TAGWs also leads to the excitation of SAGWs. Our modeling results suggest that TAGWs can drive detectable and quantifiable perturbations in the upper atmosphere, under a wide range of scenarios, but also uncover new challenges and opportunities for their observations. The results of the 2011 Tohoku-Oki tsunami case study are presented in section 3 and of parametric studies in section 4. The discussion and a summary of these investigations are provided in section 5. These results provide a platform for future studies that include comprehensive airglow and ionospheric responses, and comparisons with data.

2. Numerical Simulation Approach

For the simulation of tsunamis, we use GeoClaw model, which numerically solves nonlinear depth-averaged shallow water equations and was approved by the U.S. National Tsunami Hazard Mitigation Program for the use in modeling work (Berger et al., 2011; Clawpack Development Team, 2018; Gonzalez et al., 2011). Simulated vertical ocean surface velocities, generated by tsunamis, are used to specify lower boundary conditions for the three-dimensional nonlinear compressible neutral atmosphere Model for Acoustic-Gravity wave Interactions and Coupling (MAGIC) (Snively, 2013).

As a realistic scenario, we study one of the largest tsunamis that was generated by the 2011 M9.1 Tohoku-Oki subduction megathrust earthquake near the east coast of Honshu Island, Japan (epicenter at 38.297°N/142.373°E, 05:46:24.120 UT, U.S. Geological Survey). The earthquake rupture area was estimated as ∼400 km along-strike and ∼220 km across the width (Lay, 2018) and fault slips of 30–50 m during ∼100 s. On the shore of Japan, ocean waves reached ∼15–20 m in height with a run-up of more than 20 m (Fritz et al., 2012; Mori et al., 2011). An unprecedented amount of TAGW-driven disturbances was recorded in the Earth's magnetic field; airglow layers and ionospheric plasma densities were collected in data at the near-epicentral region (Galvan et al., 2012; Liu et al., 2011; Maruyama & Shinagawa, 2014; Saito et al., 2011) and in the far-field (Azeem et al., 2017; Hao et al., 2013; Makela et al., 2011; Yang et al., 2014, 2017).

The complexity of the earthquake motivated studies leading to a wide range of proposed finite-fault models that produce different peak vertical displacements at the seafloor ranging from 7 to 22 m (Lay, 2018). Through simulations of the Tohoku-Oki tsunami with the GeoClaw model, MacInnes et al. (2013) investigated the reproduction of wave gauge data with 10 different ITDs. Based on the analysis of their and our own modeling results, here we specify temporally varying ITD, calculated in a forward seismic wave propagation simulation with SPECFEM3D_GLOBE codes based on finite-fault model by Shao et al. (2011).

For the details of the modeling process, we refer to Inchin et al. (2020), that is devoted to the investigation of mesopause airglow responses to AGWs with the use of the same ITD.

We specify 500 m Gridded Bathymetry Data J-EGG500 with $30''$ USGS GTOPO topography near the Japan Islands area and $1'$ ETOPO1 bathymetry from the National Environmental Satellite, Data, and Information Service (NESDIS) archive for open ocean. Bottom friction is incorporated with a Manning roughness coefficient of 0.025. To avoid boundary discontinuities, we apply a smooth taper at the edges of the ITD domain prior to incorporating it into GeoClaw. ITD dynamics are resolved for 12 min after the earthquake's initiation time for the region of $1,200 \times 1,200$ km around the epicenter. The tsunami evolution is computed for 7 hr, until direct waves reach the farthest boundary of the numerical domain.

TAGW dynamics are resolved for 7 hr in a domain of $6,000 \times 5,490 \times 500$ km in latitude, longitude, and altitude directions, respectively. The horizontal and vertical resolutions are chosen as 5 and 1 km, respectively, resulting in 0.6588B grid points of the numerical domain. We apply wave-absorbing ("sponge") layers near the edges of MAGIC numerical domain to avoid boundary wave reflections. Meridional and zonal winds and temperature profiles for altitudes up to 55 km are used from the MERRA-2 database. For higher altitudes, empirical models NRLMSISE00 (Picone et al., 2002) and HWM-14 (Drob et al., 2015) are specified. MERRA-2 data are selected for 15:00:00 LT, $\sim$14 min after earthquake initiation time. The configurations of models for parametric 2D and 3D studies are provided separately in section 4.

3. Tohoku-Oki Tsunami Case Study Results

This section contains five figures that demonstrate TAGW characteristics and evolution from different perspectives, and through the whole range of altitudes, distances, and times. Figure 1 presents snapshots from the simulated ocean surface vertical velocities (panel a), and absolute major gas temperature perturbations (T'), sliced horizontally at four altitudes (panels c–f). The snapshots of T' for chosen meridional and zonal slices, shown with dashed lines in Figure 1d, are provided in Figures 1g–1l. Time-distance diagrams of ocean surface vertical velocities and T' at 50, 150, 250, and 350 km altitudes for zonal and meridional slices are presented in Figure 2. Power spectral density (PSD) diagrams for the zonal slice of the ocean surface vertical displacements and T' at four altitudes are provided in Figure 3. The bathymetry of the numerical domain, obtained through NESDIS services, and the field of maximum simulated tsunami amplitudes are presented in panels a and b of Figure 4, respectively. The fields of maximum T' from horizontal slices at 50, 150, 250, and 350 km are shown in Figures 4c–4f. The fields of maximum horizontal and vertical fluid velocities for meridional and zonal slices are depicted in Figure 5, along with the bathymetry profiles corresponding to these slices. All maximum perturbation fields are calculated incorporating the dynamics during 7 hr of simulation. The animations for the figures are provided in the supporting information (see a link to Embry-Riddle Aeronautical University Scholarly Commons repository in the Acknowledgement section).

Tsunami evolution is influenced by bathymetry variations, resulting in refraction, reflection, focusing, and branching of waves (Mofjeld, 2000; Satake, 1988). The strongest tsunami waves are simulated to the southeast of the epicentral area (Figure 4b). The propagation of the tsunami to the north and northeast is markedly affected by shallow bathymetry near the shore of Japan and the Kuril Islands. Long-lived dynamics, driven by trapped and deflected waves, are discernible near the coast of Japan (Figures 2a and 2b). Along with the shores, notable tsunami wave reflections result from the Hawaiian-Emperor Seamount Chain (HESC) to the east, Izu-Bonin-Mariana Arc (IBMA) and Ogasawara Plateau to the south and the Mid Pacific Mountains (MPM) to the southeast. Apparent focusing of tsunami waves is driven by Shatsky and Hess rises. The tsunami exhibits a broad spectrum of periods in the range of $\sim$7–60 min with a dominant peak at $\sim$19–20 min, and horizontal wavelength (λ_x) varying between 140 and 400 km (Figure 3a). The average apparent phase speed of the tsunami waves is $\sim$231 m/s, though its marked change results from bathymetry variations, for example, over Shatsky Rise or IBMA. The comparison of synthetic and Deep-ocean Assessment and Reporting of Tsunami (DART) wave gauge data is provided in Figure 1b.

The strongest perturbations in the atmosphere are generated over the epicentral area by strongly nonlinear acoustic waves (AWs) from intense ocean surface displacements over crustal deformation (Figure 5). In this area, the perturbations are present even 5 hr after the earthquake (Figures 1f, 2i, and 2j) and exhibit periods of $\sim$4.2 min (Figure 3) and result from AWs that are trapped between the ground and lower thermosphere, tunneling to higher altitudes (Figures 1f, 1g, 1i, and 2h). Similar long-lived dynamics were observed for at least 4 hr after the earthquake in total electron content (TEC) data (Saito et al., 2011; Tsugawa et al., 2011).
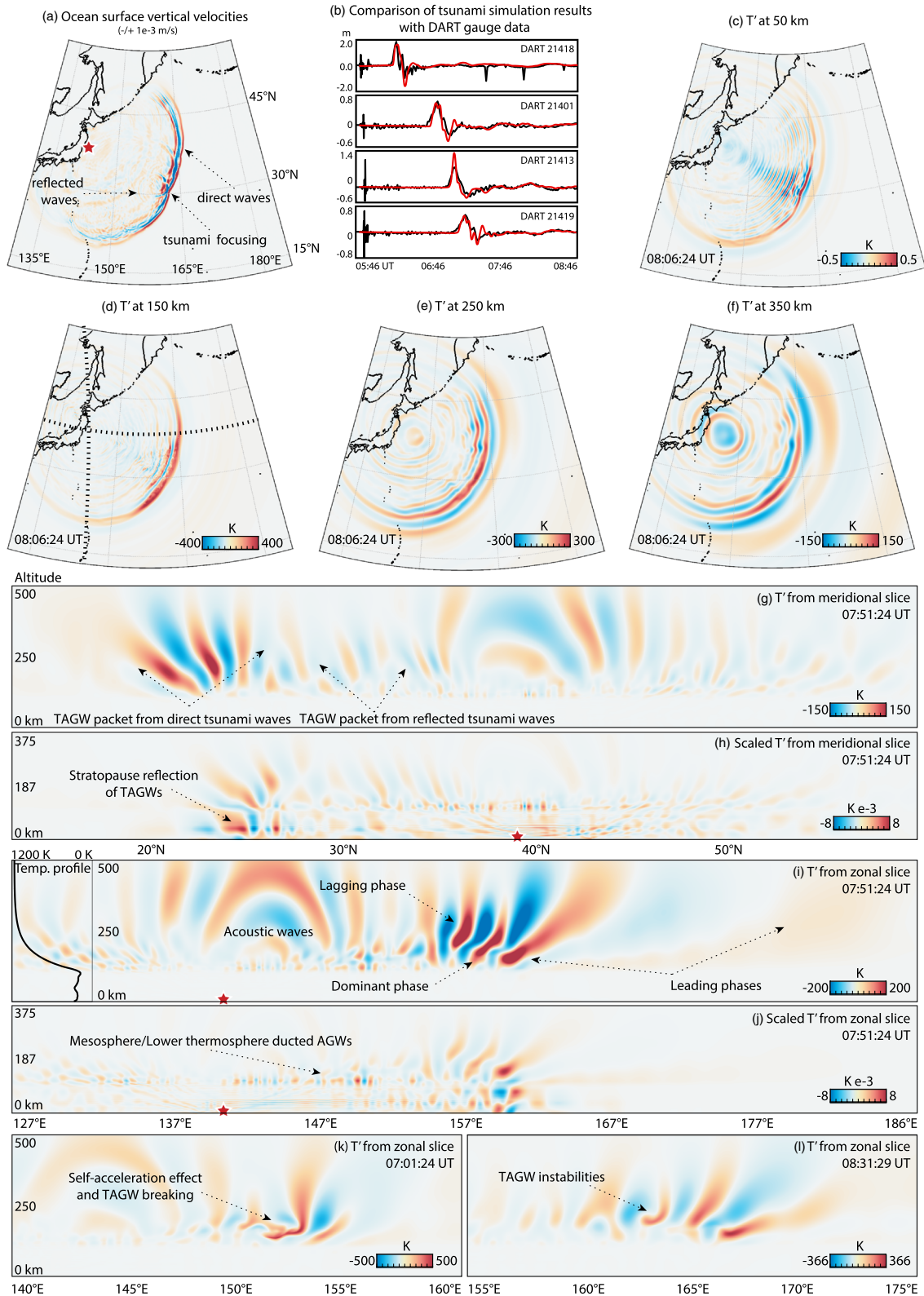
Figure 1. The snapshots of (a) ocean surface vertical velocity and (c–f) T' at four altitudes; (g–l) absolute and scaled T' for meridional and zonal slices shown with dashed lines on panel d. (b) The comparison of simulated ocean surface vertical displacements with DART wave gauge data. The data on plots are presented on an oversaturated scales for better visibility of weaker features.
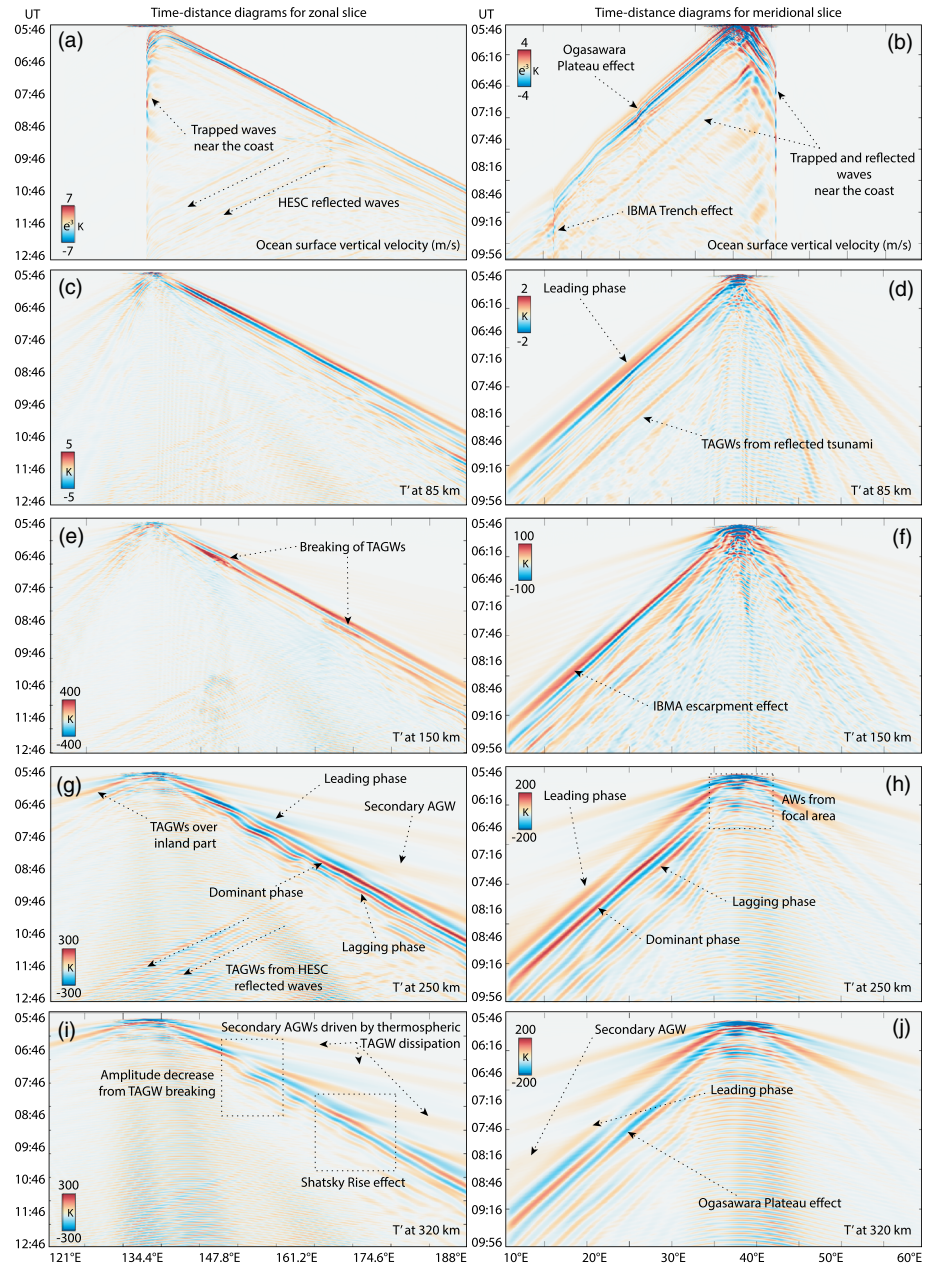
Figure 2. Time-distance diagrams of (a, b) ocean surface velocity and (c–j) T' for zonal (left column) and meridional (right column) slices at four altitudes. Chosen slices are shown with dashed lines in Figure 1d. The data on plots are presented on an oversaturated scales for better visibility of weaker features.

With time, the simulated AWs are slightly shifted to the east from the epicentral area, that is explained by the dominant eastward wind from ground to ∼110 km height (wind profiles are provided on Figures 5a and 5d). It should be noted that the resolution of the numerical grid is suitable primarily for TAGW dynamics to meet computational expenses, whereas short-period AWs can be underresolved. AW dynamics and generated mesopause airglow perturbations, driven by this ITD, were discussed by Inchin et al. (2020).

TAGW packet structure is preserved for the whole range of distances and altitudes (Figures 1g–1l). Notable leading phases in the TAGW packet exhibit periods of ∼25–45 min and propagate ahead of the tsunami (Figures 1c–1j, 2d, 2g, 2h, and 2j). Possessing substantial amplitudes from the ground to the lower thermosphere, they experience marked damping above ∼150 km, having comparatively small vertical wavelengths (λ_z) of ∼150–200 km (λ_x ∼250–500 km), leading to their dissipation at lower altitudes (Vadas, 2007).
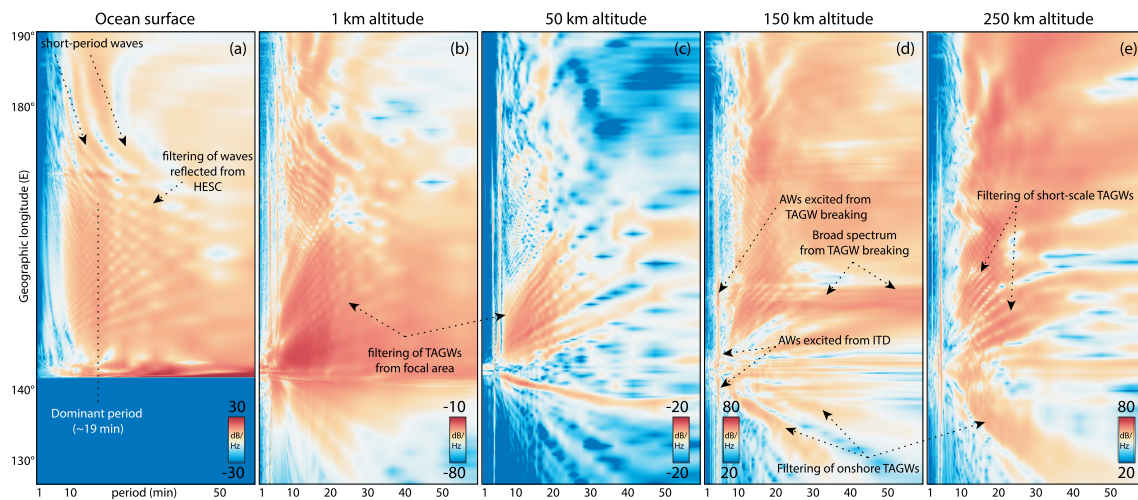
Figure 3. Power spectral density (PSD) diagrams of ocean surface vertical displacements and T' at four altitudes, derived by calculating PSD for each position of the zonal slice shown on Figure 1. The data on plots are shown on an oversaturated scales for better visibility of weaker features.

The dominant TAGW phase, slightly trailing behind the tsunami wavefront, is locked with a dominant tsunami period of ~19 min (at thermospheric heights, its $\lambda_x \sim 260$ km, $\lambda_z \sim 260$ km, and $v_z \sim 228$ m/s) and in general exhibits stronger amplitudes above lower thermosphere than leading phases (Figures 2g–2j). From the ground to the mesosphere, its amplitude is usually lower than of the leading phases, though marked variations are present at all altitudes (Figures 4g and 4i). The next trailing phase front has comparatively short $\lambda_x \sim 190$ km, but large $\lambda_z \sim 300$–330 km in the thermosphere and may exhibit substantial amplitudes at ionospheric heights, but does not produce any notable perturbation below the thermosphere. The following train of TAGWs includes ducted and resonating waves, as well as TAGWs from refracted and reflected tsunami waves, spanning a broad range of periods, though with some components of comparatively small amplitudes.

Thermo-viscous molecular dissipation of TAGWs at thermospheric heights, and transience within the tsunami-driven wave field, are causes for the local generation of SAGWs. They propagate ahead of the TAGW packet with an apparent horizontal phase velocity (v_x) of ~600 m/s and exhibit amplitudes up to ~50 K (Figures 1f and 1g). A particularly strong SAGW is generated from the epicentral region and propagates practically through the whole numerical domain. SAGWs have large λ_x of ~600–700 km and periods of ~14–18 min. Our results demonstrate at least superficial agreement with a previous study by Kherani et al. (2015), who reported similar characteristics of these SAGWs. It is interesting to note that the local generation of SAGWs (from the transience within the tsunami-driven wave field) occurs most prominently as TAGWs packet tilts horizontally from the change of wave intrinsic frequency. Commonly, the enhancement of leading phases in the thermosphere is followed by the radiation of SAGWs (Figures 2g and 2i).

At thermospheric heights, TAGWs exhibit temperature perturbations of ~100–250 K, though some local peaks reach 600–700 K at 150 km altitude (Figure 4b). Vertical fluid velocities, starting from lower thermosphere, vary in a range ~150–200 m/s, whereas horizontal fluid velocities are ~150 m/s on average. The phase speeds of the tsunami and TAGWs at altitudes lower than ~100 km are practically the same ~231 m/s (Figure 2c) and TAGWs exhibit similar amplitude variations as the tsunami (Figure 4c). At thermospheric heights, there is a notable variability of TAGW phase speeds (Figures 2g–2j) and amplitudes (Figures 4d–4f), which result from bathymetry variations and nonlinear effects (nothing that fluid velocities are comparable to the phase velocity). Although the dispersive nature of the TAGW packet also leads to its spreading (Laughman et al., 2017), this effect takes relatively longer distances prior to becoming clearly discernible.

The gap in the fields of maximum perturbations at ~300–500 km radially from the epicenter, where practically no perturbations are observed in the upper atmosphere, is explained by the distances that need to be covered by TAGWs before they reach upper layers (Occhipinti et al., 2013). Then, the strongest TAGWs propagate at distances 500–800 km to the southeast from the epicentral region and are driven by the substantial amplitudes of the tsunami near its source (Figures 4b and 4g). The leading phases exhibit comparatively strong amplitudes at ~153°E and ~130–150 km altitudes. The following trailing phases appear in the lower
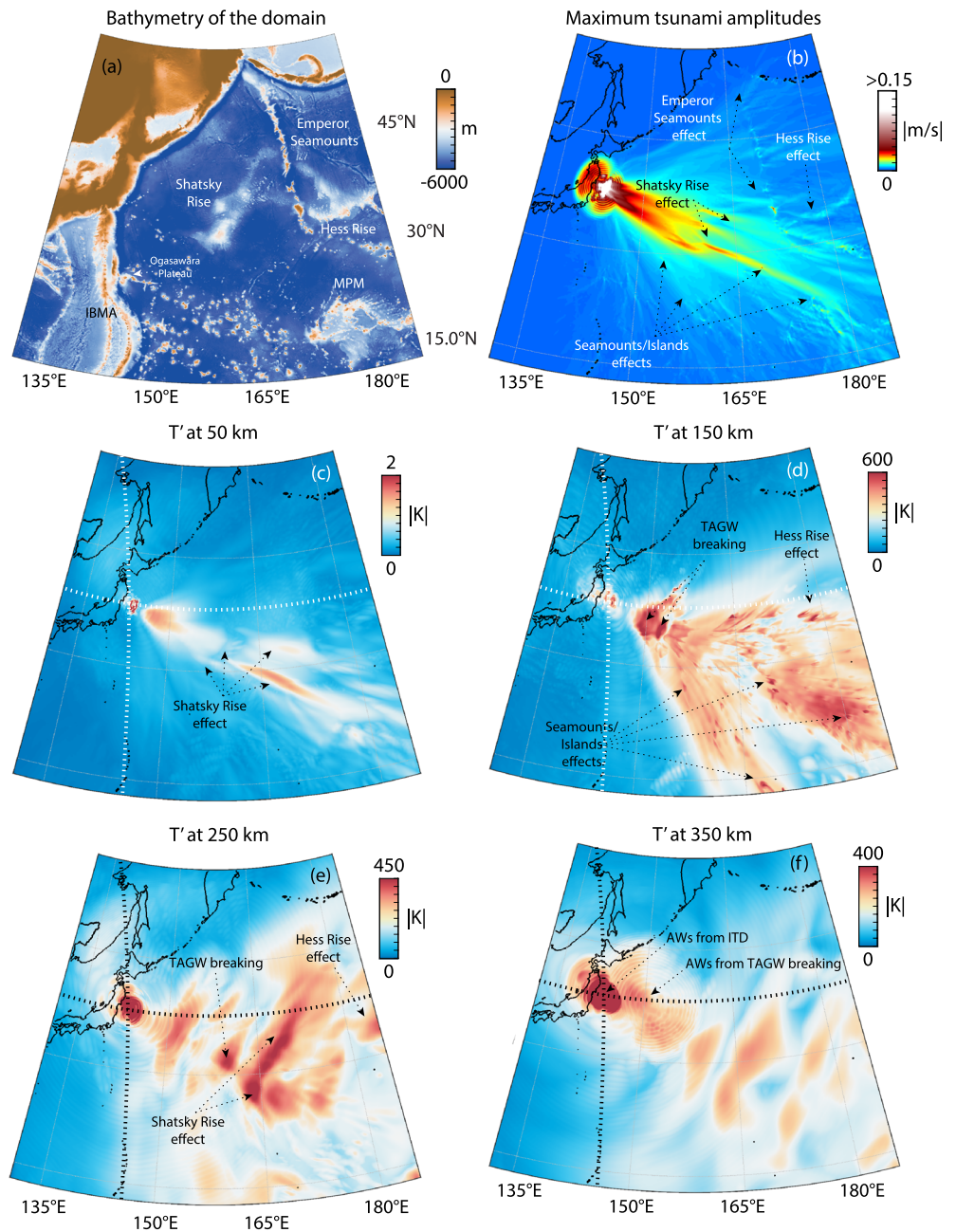
Figure 4. (a) Bathymetry of the numerical domain. (b) The field of maximum simulated vertical ocean surface velocities. (c–f) The fields of maximum T' at four altitudes. The data on plots are shown on an oversaturated scales for better visibility of weaker features.

thermosphere already with practically vertically aligned phase fronts and apparent instabilities arise right after them (Figure 1k). Leading phases induce mean flow and increase local v_x (Figure 5d), which results in the horizontal acceleration of trailing phases in the direction of TAGW packet propagation, that start exhibiting larger v_z and subsequent phase front distortions. As the speed of the mean flow exceeds phase velocities of TAGWs, breaking of waves occurs. Further to the southeast, apparent breaking of trailing phases of the TAGW packet occurs, but at altitudes of ~200 km (Figure 1l). Again, prior to breaking, trailing phases start tilting vertically as they are shifted to higher intrinsic frequencies and larger λ_z. At 150–200 km altitudes, the amplitudes of leading phases are already comparatively small, and we attribute instabilities to the induced mean flow by the dominant phase.

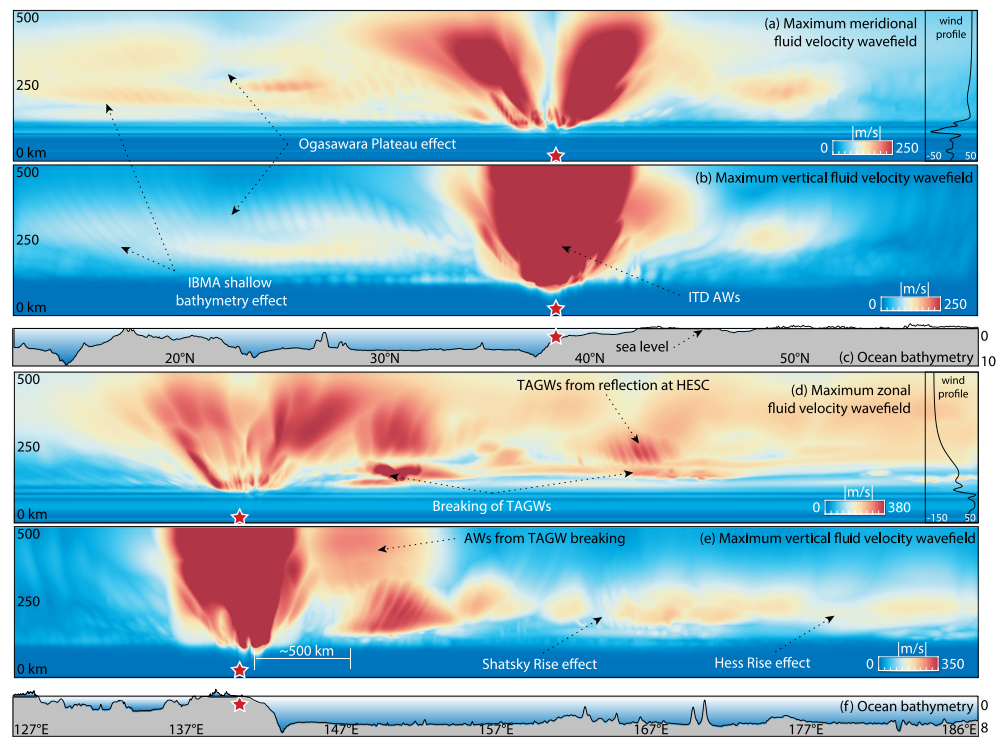**Figure 5.** Fields of maximum elongated and vertical fluid velocities for (a, b) zonal and (d, e) meridional slices shown with dashed lines on Figure 4b. (c, f) Bathymetry profiles for chosen meridional and zonal slices. The data on plots are shown on saturated scales.

The dynamics discussed above support the conclusion that the simulated instabilities arise via self-acceleration effects from strong mean flow, induced by the leading phases of the TAGW packet (Dong et al., 2020; Fritts & Lund, 2011; Fritts et al., 2015). Along with the generation of long-period SAGWs, TAGW breaking leads to the generation of AWs (e.g., Snively, 2017, and references therein) that drive long-lived dynamics (Figures 3d, 4f, 5d, and 5e). The TAGW breaking may be in part enhanced from the interaction of TAGWs excited by direct tsunami waves and TAGWs from tsunami waves that are first reflected from the coast of Japan and then closely follow direct tsunami waves (Figure 1a). As TAGWs from direct tsunami slow down over the Shatsky Rise, they can more readily interact with the TAGWs from the reflected tsunami.

The spreading of ocean waves over the passage of Shatsky Rise leads to the decrease of their amplitudes, but focusing intensifies the tsunami to the east and southeast (Figure 4b). At altitudes lower than ∼100 km, TAGWs practically mimic the tsunami evolution (Figure 1c). They exhibit similar initial decrease and further enhancement of amplitudes, and two intensified region of T' to the southeast and east can be discerned (Figure 4c). In the lower thermosphere, the Shatsky Rise produces similar effects, although less prominent. At 250 and 350 km, there is no elongated southeastward enhancement of TAGWs, but, instead, the pattern of perturbations practically mimics the shape of the Shatsky Rise from Tamu Massif at the southwest to Shirshov Massif at the northeast (Figures 4a, 4e, and 4f). We attribute this enhancement in the perturbations to TAGW self-acceleration and following instabilities from tsunami passage over the Shatsky Rise and its focusing. Also, perturbation enhancement is accompanied by substantial increase of horizontal fluid velocities in these regions (Figure 5d).

In a north-south direction and meridional slice shown with a dashed line in Figure 1d, TAGWs possess comparatively smaller amplitudes (∼150–200 K) and do not display significant nonlinearity, in contrast to the east and southeast, and no apparent TAGW instabilities occur. Here, even at 150 km altitude the leading phases exhibit the strongest amplitudes (Figures 2d and 2f). At higher altitudes, the dominant phase exhibits the strongest amplitudes and the trailing phases are practically absent at ionospheric F-layer (Figures 2h and 2j). After the passage of Ogasawara Plateau, the TAGW trailing phase amplitudes are decreasing locally, while TAGW leading phases are enhanced (Figure 2j). Over shallower bathymetry, the tsunami speed decreases, followed by the diminishing of λ_z of TAGWs. The whole TAGW packet tilts horizontally and the

leading phases intensify (though are still damped at ionospheric heights drastically), whereas trailing phases start dissipating at lower altitudes. This can be seen from the increase of the meridional fluid velocities (from the intensified leading TAGW phases) at altitudes lower than ~200 km and the diminishing of vertical fluid velocities and T' above ~250 km (Figures 5a and 5b). Notable decrease of vertical, and the enhancement of horizontal, fluid velocities can also be seen farther to the south, as the tsunami runs into a shallower bathymetry of IBMA and the TAGW packet tilts horizontally.

The reflections of the tsunami from the HESC result in ocean surface waves and TAGWs of notable amplitudes as they return to the Japan coast (Figures 2a and 2g). This is supported by observed TEC perturbations from these reflected waves (Tang et al., 2016). The arrival of the simulated and observed reflected TAGWs from the HESC to the shore of Japan is ~6 hr after the earthquake. Simulated T' of these TAGWs reach ~100–140 K at 250 km. The reflection and refraction of tsunami waves from the HESC leads to the excitation of short-scale waves in the ocean and subsequently short-scale TAGWs in the atmosphere (Figure 3), which transit to longer periods away from HESC. Notable tsunami reflections to the north from the epicentral area result in a second TAGW packet that follows the TAGW packet generated by direct tsunami waves propagating to the south (Figure 1g). These two packets are spatially separated and do not interact.

The interaction of the tsunami with seamounts and islands leads to the generation of compact but markedly intensified short-scale TAGWs (Figure 4d). These TAGWs are particularly apparent to the east of the IBMA in a quadrant 15–30°N and 150–165°E (Figure 4b). However, they are markedly attenuated at higher altitudes and are practically not present at 250 km (Figure 4e). In the southeast quadrant of the domain, the perturbations are absent at almost all altitudes, which is caused by tsunami damping from the interaction with the MPM. Notable perturbations at 50 and 150 km follow the same way to the north from the MPM as the tsunami (Figures 4c and 4d), but this evolution is practically not present at 250 and 350 km.

Finally, the evolution of the tsunami with distance leads to the filtering of small-scale ocean waves and TAGWs, as can be seen in the zonal direction between 142°E and 160°E in Figure 3. Over the inland part, in the absence of a quasi-continuous source (tsunami), the TAGW energy peak is shifting from shorter to longer periods and horizontal scales. Dissipative filtering drastically affects TAGW phases with longer λ_z (Heale et al., 2014), but even 10° to the west, the power of TAGWs is still substantial at thermospheric heights (Figures 3d and 3e).

4. Effects of ITD and Bathymetry on TAGWs

The 2011 Tohoku-Oki tsunami case study shows that bathymetry variations may markedly affect the amplitudes and characteristics of TAGWs. In this section, we continue this analysis based on simulations with simplified and demonstrative bathymetry variations and ITDs.

We use a single 1D or 2D circular Gaussian model as the ITD:

$$ITD(x_i, y_j) = A \cdot e^{\left(-\frac{(x_i - x_c^2)}{2\sigma^2} - \frac{(y_j - y_c^2)}{2\sigma^2}\right)}, \tag{1}$$

where the ITD is set as instantaneous, x_c, y_c the position of the center of the peak, σ the standard deviation, and A the amplitude, set as 0.6 m. Tsunami dynamics for the 2D TAGW simulations are calculated in the Cartesian 1D version of GeoClaw. The species densities and temperature profiles are utilized from the Tohoku-Oki case study. Winds are not included in these idealized simulations to control complexity.

We start with the investigation of the effect of ITD size on TAGWs. Figures 6a–6d show the simulation results of TAGW dynamics generated by four different tsunamis with λ_x = 107, 154, 214, and 297 km and periods 9, 13, 18, and 25 min, respectively. The bathymetry is set as flat at 4 km depth and the amplitudes of ITDs are decreased by a factor of 100, in order to exclude nonlinear effects. For each case, we provide an x-z snapshot of T' and a corresponding 2D wavelet of λ_z, time-distance diagram of T' at 320 km, and λ_x and period wavelets for slices shown with blue lines on time-distance diagrams. The data on the time-distance diagrams are shown with saturated color scales for better visibility of weaker features and the maximum and minimum values are indicated. As expected, tsunamis of different periods result in different dominant intrinsic frequencies and thus phase velocities of the TAGW packet. The amplitudes of the long-period leading phases that reach 320 km become notable with the increase of the tsunami period, while trailing phases are more apparent with the decrease of the tsunami period. In common, shorter period tsunamis result
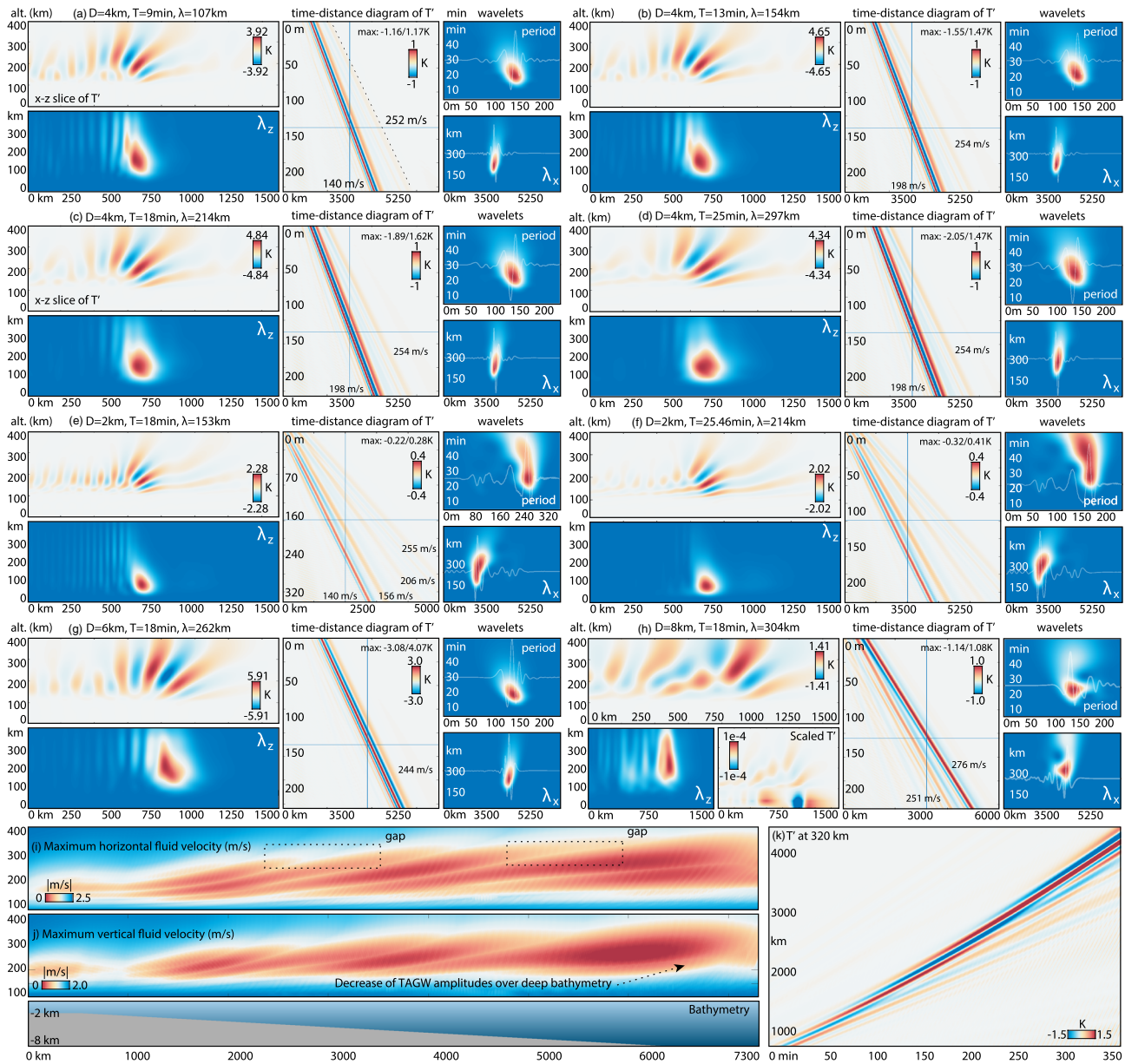
Figure 6. (a–h) The results from eight parametric simulations presented with altitude-distances (x-z) slices of T' and corresponding λ_z 2D wavelets, travel-time diagrams of T' at 320 km, as well as λ_x and period wavelets for slices at 320 km shown with blue lines on travel-time diagrams. Values in travel-time diagrams indicate horizontal apparent phase velocities. (i–j) Fields of maximum horizontal and vertical fluid velocities from the simulation with constantly decreasing bathymetry. (k) Time-distance diagram of T' at 320 km altitude.

in weaker TAGWs in the thermosphere. TAGW dominant λ_z varies in the range ~147–156 km in the thermosphere, whereas λ_x increases markedly with the increase in a tsunami period, from 206 km for a 9 min period tsunami to 264 km for a 25 min period tsunami. Thus, the spectra of the tsunami waves and their coupling with AGWs clearly establishes the observable spectrum in the atmosphere (Vadas et al., 2015; Wu et al., 2016, 2020).

Panels c, e, g, and h of Figure 6 show simulation results of TAGW dynamics generated by a tsunami with a dominant period of 18 min that propagates over flat bathymetry of 2, 4, 6, and 8 km depth. To recall, the propagation of the tsunami over different depth of the ocean results in a change of its λ_x and v_x, as the tsunami speed for the shallow-water approximation is $v_x = \sqrt{gH}$, where g is the Earth's gravity and H is the ocean depth. This in turn leads to the change of dominant phase velocities and horizontal wavelengths (and thus frequencies) of the generated atmospheric TAGWs. Shallower bathymetry results in shorter

tsunami's λ_x, and a shortening of dominant thermospheric λ_z of TAGWs, from 236 km in case of 8 km depth to 92 km for 2 km depth. Shallow bathymetry are causes for a notable presence of leading TAGW phases due to the decrease of dominant intrinsic frequencies of generated in the atmosphere TAGWs, even at 320 km, that exhibit comparable amplitudes to the dominant phase (Figure 6e). In case of deep bathymetry, leading phases are practically not present in the thermosphere, but trailing phases appear. The maximum TAGW amplitudes at thermospheric heights are 2.28, 4.84, 5.91, and 1.141 K for 2, 4, 6, and 8 km depth bathymetry, respectively. In case of 8 km bathymetry, practically all phases are evanescent starting from the stratosphere (scaled T' snapshot is provided in Figure 6h). Although at thermospheric heights some of these phases are freely propagating, they exhibit small amplitudes. The dominant λ_x at 320 km varies from $\sim$270 km for 2 km depth to $\sim$230 km for 6 km depth bathymetry.

In Figure 6i–6k, we provide simulation results with gradually increasing ocean depth from 2 to 8 km over 7,300 km distance. As it is stated earlier, the excitation and dynamics of TAGWs are defined by the dominant phase velocities and horizontal wavelengths imposed by the tsunami, which in this case are constantly increasing width depth. This results in a wide range of characteristics of TAGWs and their amplitudes, leading up to the onset of evanescence, what can be seen from panels i and j that demonstrate continuous change of horizontal and vertical fluid velocities of TAGWs. This can also be seen in the time-distance diagram of T' at 320 km shown in Figure 6k. At some time epochs, two phases may exhibit similar amplitudes at one altitude. The TAGW packet lines of constant phase tilt increasingly vertically with increasing ocean depth and increase of the intrinsic frequency. In general, TAGWs drive stronger perturbations at higher altitudes as the ocean depth increases. However, it is not the rule; for example, fluid velocities decrease at $\sim$250–300 km altitudes at distances of $\sim$2,500 and $\sim$5,500 km. Over some depth, the tilting TAGW packet may provide fairly small perturbation at these heights when it dissipates at lower altitudes (i.e., where thermo-viscous dissipation starts dominating wave amplitude growth from the decrease of atmospheric mean density). As the bathymetry reaches a depth of $\sim$7 km or deeper, TAGWs in the thermosphere start to lose intensity, as most of the generated TAGWs are evanescent at altitudes lower than 100 km.

Next, we address the bathymetry effect based on 2D simulations with simplified ocean floor variations. The snapshots of absolute and scaled T' are present in Figure 7. Distance-altitude plots show TAGW dynamics after the passage of bathymetry feature (variation) that is located at $x = 0$ km. Except bathymetry features, the depth of the ocean is set as 4 km in all simulations. The ITD generates a tsunami with $\lambda_x \sim 214$ km, as shown in panel c of Figure 6, but here its amplitude peaks at 0.6 m height. For the demonstration of how ocean floor variations affect TAGWs, we separately provide simulation results with flat bathymetry in Figure 7a, and in this case, T' reaches $\sim$191 K in the thermosphere.

Arcs and chains of seamounts cause a marked change of tsunami characteristics, reflection, and trapping of waves. We present simulation results with different shapes of arcs. A narrow arc is represented with a Gaussian function with $\sigma = 70$ km and a wide arc, comparable with the Tamu Massif of Shatsky Rise, is represented by a Gaussian function with $\sigma = 300$ km. A plateau is represented by a bathymetry depth change from 4 to 0.5 km with uplift and downlift of 31 km and plateau extension of $\sim$267 km using a tapered cosine function (applicable for the representation of the plateau):

$$ITD(x) = \begin{cases} \frac{1}{2}\left\{1 + \cos\left(\frac{2\pi}{r}\left[x - \frac{r}{2}\right]\right)\right\}, 0 \le x < \frac{r}{2} \\ 1, \frac{r}{2} \le x < 1 - \frac{r}{2} \\ \frac{1}{2}\left\{1 + \cos\left(\frac{2\pi}{r}\left[x - 1 + \frac{r}{2}\right]\right)\right\}, 1 - \frac{r}{2} \le x < 1 \end{cases}, \tag{2}$$

where r represents cosine fraction and set as 0.25 (Figure 7f). The narrow arc barely affects TAGW propagation, with only localized enhancement of the leading phases and diminished amplitudes of the dominant phase (Figure 7b). However, in case of wide arc, initial TAGW packet markedly dissipates prior to a newly formed TAGW packet (formed from waves after arc passage) appears at later time epochs and distances (Figure 7c). After the formation of the new TAGW packet, slowly dissipating leading TAGWs from the initial packet may still generate notable perturbations over $\sim$100–1,500 km distances. Tsunami propagation over the wide arc also results in a local generation of TAGWs that can be discerned at 85 km, but they are weak at thermospheric altitudes. In the case of tsunami propagation over the flat plateau, parts of the tsunami waves are reflected back from the plateau uplift and generate TAGWs propagating toward the ITD. Trapped and propagating over the plateau tsunami waves generate short-scale TAGWs that are practically all dissipated below the thermosphere.
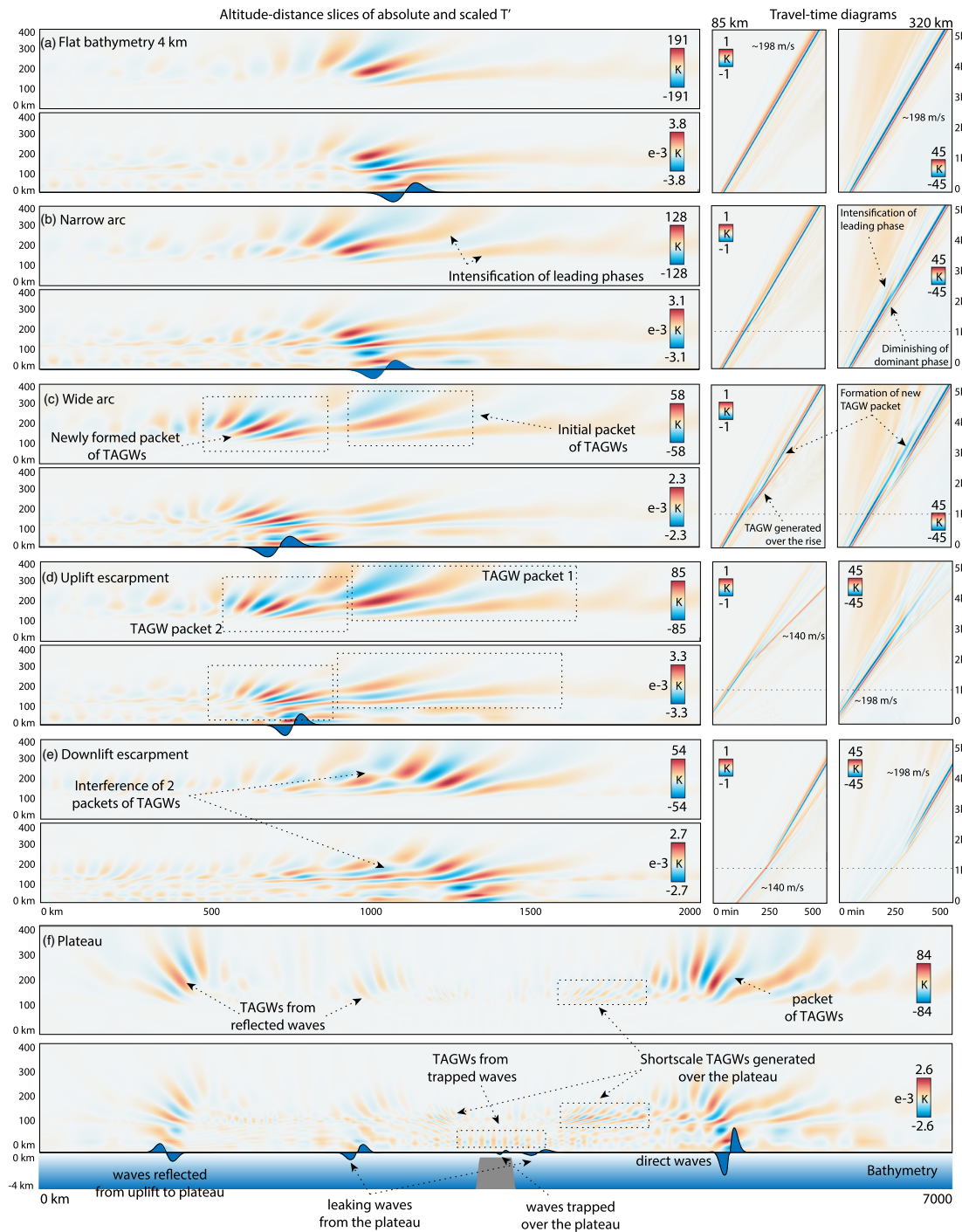
Figure 7. (a–e) Altitude-distances slices of absolute and scaled T' and travel-time diagrams of absolute temperature perturbations at 85 and 320 km for bathymetry variation cases. Numbers of travel-time diagrams indicate horizontal apparent phase velocities in m/s. (f) Altitude-distance slices of absolute and scaled T' for the case of simulation with plateau.

In panels d and e of Figure 7, we show the result of simulations with uplift and downlift escarpments with 2 km depth variation over 75 km distance. Such escarpments are present, for example, at IBMA, Tonga Ridge, Ryukyu Arc, and shelfs. The TAGW packet, driven by the tsunami prior to reaching the escarpment, continues propagating in the same direction. Without continuous forcing by the tsunami, these TAGWs disperse and dissipate, transitioning the packet toward larger dominant λ_x. The newly formed TAGW packet appear ~400 and ~600 km ahead of the escapement at 85 and 320 km altitudes, respectively. As this packet tilts
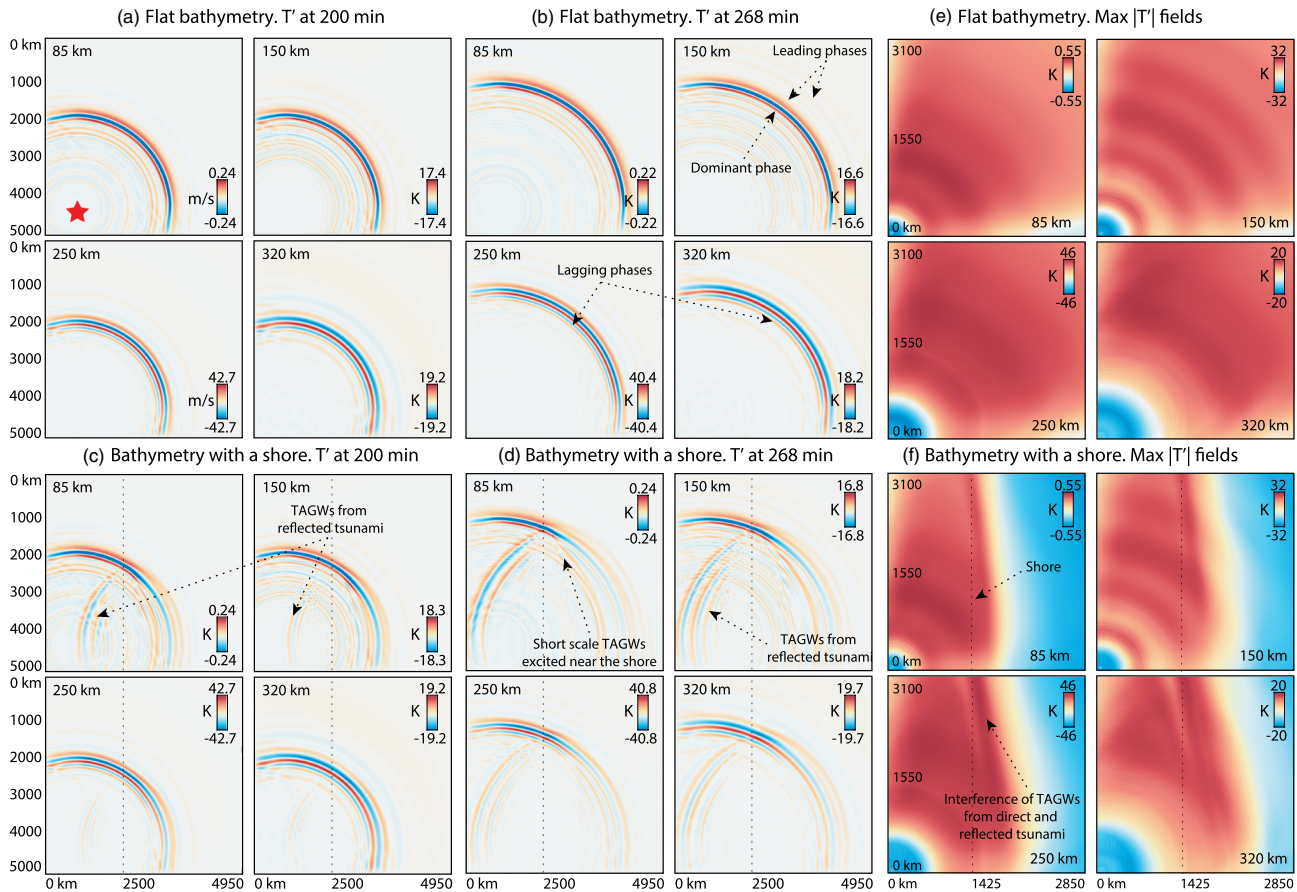
Figure 8. The snapshots of sliced horizontally T' at four altitudes from simulation with (a, b) flat bathymetry and (c, d) bathymetry with a shore, shown with dashed vertical lines. (e, f) The fields of maximum T' at four altitudes for (e) flat bathymetry simulation and (f) bathymetry with a shore.

horizontally (exhibiting lower intrinsic frequency) over shallow bathymetry, the maximum TAGW amplitudes at 85 km height enhance from 0.55 to 0.8 K, whereas at 320 km, TAGW amplitudes fall drastically from 40 to 9.8 K. The reverse situation is present after the passage of the downlift escarpment, where TAGW amplitudes become smaller at 85 km (from 0.51 to 0.46 K) and larger at 320 km height (from 6.46 to 22.78 K).

Next, we present simulation results of continued TAGW propagation over land, as the tsunami reaches the coast (Figure 8). The chosen ITD generates a tsunami with a dominant period of ~18 min and λ_x~214 km over flat bathymetry of 4 km depth. First, for reference, we demonstrate the 3D simulation with flat bathymetry of 4 km depth (Figures 8a, 8b, and 8e). TAGWs, generated over flat bathymetry, propagate concentrically away from the source. The generation of SAGWs in the thermosphere, propagating ahead of the TAGW packet, can be seen. Again, the leading phases are more prominent at lower altitudes, whereas phases with larger λ_z dominate in the thermosphere. The fields of maximum T' perturbations are not uniform, as TAGWs disperse spatially and excited SAGWs propagate separately (Figure 8e). Next, a straight-line shore is set as a transition of ocean depth from 4 to 0 km over 45 km extension. The shore is shown in Figures 8c, 8d, and 8f with a dashed line. The distance between ITD and the shore is set as 2,000 km in a straight direction. The propagation of TAGWs over land leads to comparatively fast filtering of the dominant and trailing phases that possess longer λ_z (Figures 8c and 8d). As it was demonstrated by Heale et al. (2014), this filtering is driven by faster dissipation of phases with larger v_z, that reach thermospheric heights earlier and dissipate first. Far inland, the leading phases of the TAGW packet start exhibiting the largest amplitudes. In the vicinity to the shore, the packets of small-scale TAGWs are excited and are driven by shortening of the tsunami wavelength as it reaches the shore, although they dissipate below ~200 km altitude.

As the tsunami approaches the shore obliquely, reflected and direct tsunami waves interfere at the vicinity of the shore, producing an obliquely nonuniform region of ocean surface displacements. The same pattern can
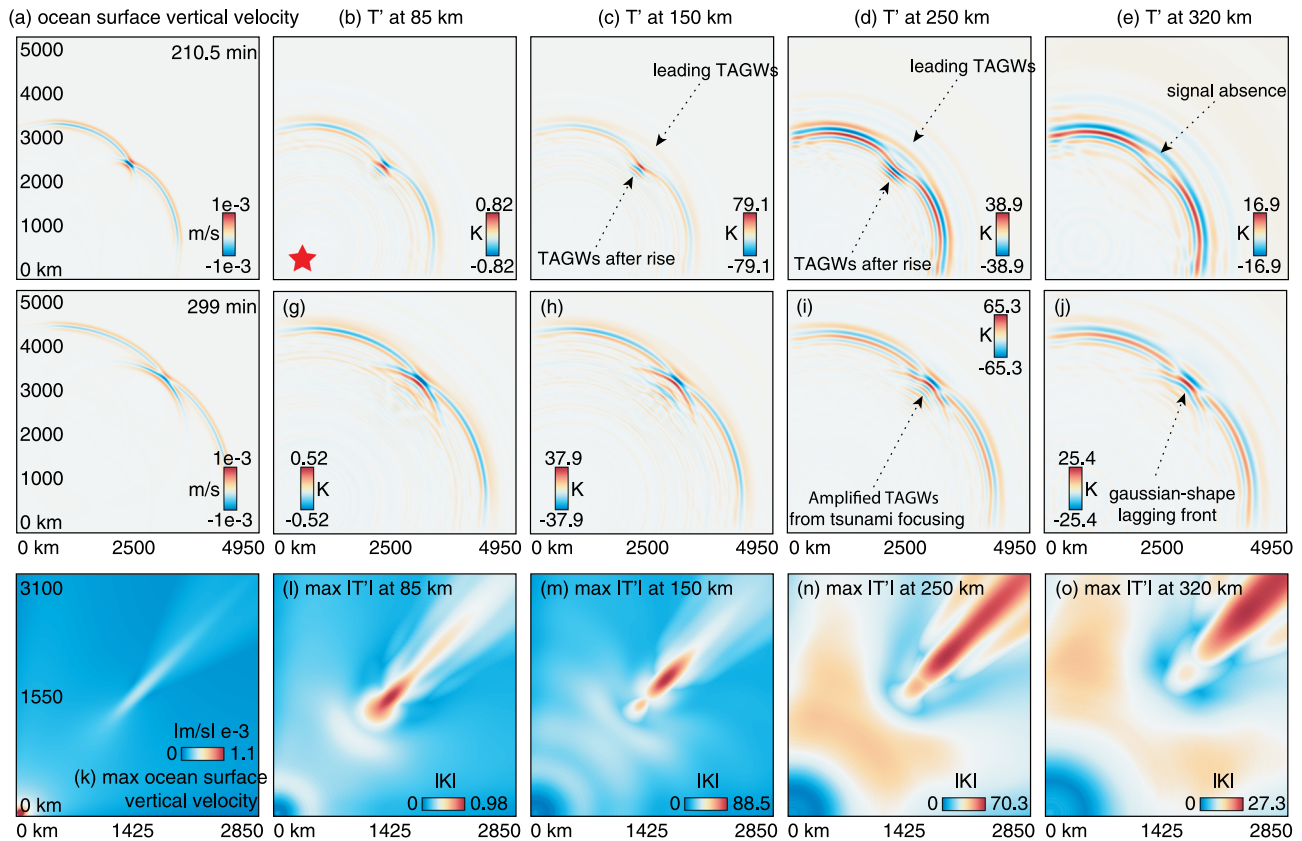
Figure 9. The snapshots of (a) ocean surface velocity and (d–e) sliced horizontally T' at four altitudes from simulation with rise presence. Time epochs of snapshots are indicated on panel a. (e, f) The fields of maximum ocean surface vertical velocity and T' at four altitudes.

be seen in the TAGW fields of maximum perturbations at distances 100–500 km to inland part, where constructive and destructive interference of TAGWs leads to alternating regions of enhanced and diminished perturbations. At 85 km altitude, TAGW amplitudes decrease rapidly as they propagate over land, exhibiting ∼50% lower amplitudes 500 km and ∼85–88% lower at distances 1,000 km on shore. TAGWs in the thermosphere dissipate with a much slower rate. At 320 km altitude and distances 500 km on shore, TAGWs still exhibit practically the same amplitudes as near the shore, and 1,000 km on shore they fall to ∼30–50%.

Finally, based on the 3D simulation, we demonstrate the effect of tsunami focusing on TAGW evolution. For the investigation of the focusing effect, we set a rise using a single circular Gaussian model of 300 km diameter, which roughly represents the Tamu Massif of Shatsky Rise. The peak of the rise is at 2 km depth, whereas the area around is set as flat with 4 km depth. The snapshots in Figures 9b–9e present the simulated T', sliced horizontally at four altitudes. Tsunami evolution for the same time epochs are provided in Figure 9a and the maximum tsunami vertical velocities and maximum T' at 85, 150, 250, and 320 km are provided in Figures 9k–9o.

As they pass over the rise, the tsunami waves become superposed in the vicinity of a cusped caustic (Figure 9g). Such evolution is discussed by Berry (2007), and we find similar dynamics in the case of the Tohoku-Oki tsunami focusing from Shatsky Rise. TAGWs also exhibit correlated dynamics at higher altitudes, for example, at 85 and 150 km where they are superposed, leading to their amplification and interaction. Initially, the central part of the TAGW front bends while propagating over the rise (Figures 9b and 9c); then, enhanced TAGWs arise inside the caustic from the superposition of waves (Figures 9g and 9h). At altitudes of 250 and 320 km, the bending of the TAGW front is followed by an initial marked decrease of TAGW amplitudes (from the tilting of TAGW packet horizontally due to the decrease of intrinsic frequency) and at some distances, the signal is practically absent (Figure 9e). Later on, focusing of TAGWs can be seen inside the caustic (Figures 9i and 9j). Leading components of the TAGW packet, formed prior to the passage of the rise, can be discerned, propagating ahead of the newly formed TAGW packet (Figure 9j).

Tsunami focusing results in wave amplification and subsequent intensification of generated TAGWs (Figure 9k). At 150 km, TAGW amplitudes increased to almost three times the original value and reach 88.5 K in direct distances after the passage of the rise (Figure 9m). At higher altitudes, TAGWs enhance to 1.3–1.5 times their initial amplitudes and reach 70.3 K at 250 km and 27.3 K at 320 km (Figures 9n and 9o). Again, as in the case of the Tohoku-Oki tsunami, we see that TAGWs mimic the evolution of the tsunami at 85 km, whereas at higher altitudes, the amplitude variations exhibit more complex patterns. Although we demonstrate focusing of a comparatively small tsunami, such a strong amplification of TAGWs clearly indicates that, in case of large tsunamis, this amplification can readily lead to localized nonlinear effects and TAGW breaking.

5. Discussion and Conclusion

Through numerical simulations, we investigated the dynamics of acoustic and gravity waves generated by tsunamis. Simulated nonlinear ocean surface wave evolutions are used as a source of acoustic-gravity waves in the three-dimensional compressible and nonlinear neutral atmosphere model. We performed a case study of the 2011 Tohoku-Oki tsunami, as well as parametric numerical studies with demonstrative bathymetry variations and initial tsunami distributions. This section summarizes the main outcome of these studies. The TAGW packet has discernible structure, with phase variations from long-period (and long λ_x) phases at the head of the packet to short-period (and short λ_x) phases in its tail. The dominant phase is locked to the dominant tsunami phase velocity. This supports earlier findings by Vadas et al. (2015) on TAGW packet excitation as a mix of discrete and continuum spectral components, both above and below the fundamental mode. The tsunami continuously generates TAGWs in the atmosphere, representing a quasi steady-state forcing (analogous to a moving, evolving mountain; e.g., Nappo, 2013). Thus, phases in the tail of TAGW packet with larger λ_z do not dissipate earlier, as in the case of source-free propagating AGWs, where trailing short-period phases reach higher altitudes and dissipate earlier (Heale et al., 2014). Phases in the tail of the TAGW packet usually exhibit stronger amplitudes at thermospheric heights than the leading phases, whereas at lower altitudes, the leading phases may dominate.

Slower (faster) tsunamis or their deceleration (acceleration) over bathymetry features leads to a horizontal (vertical) tilt of the whole TAGW packet as its intrinsic frequency varies. This leads to the change of dissipation altitudes of components in the packet, which in turn leads to the variations of phase fronts that drive the strongest perturbations at different altitudes. The dominant phase, locked with a dominant tsunami phase velocity, does not necessarily provide the strongest signal. For example, in a shallow bathymetry case (or long period tsunami), the dominant phase amplitude can be comparable with amplitudes of the leading phases even at ionospheric altitudes, whereas deep bathymetry result in the absence of the leading phases above lower thermosphere. Although very deep bathymetry drives higher intrinsic frequency TAGWs into the atmosphere (as the tsunami propagates faster), the resulting TAGWs become evanescent in the stratosphere. With 8 km bathymetry, practically all phases from the TAGW packet are evanescent, in some cases tunneling upward and becoming propagating in the thermosphere (e.g., Snively & Pasko, 2008, and references therein). Indeed, as it was demonstrated by Wei et al. (2015), there is a barrier of $2NH < V < c$ (N = Brunt-Väisälä frequency, H = scale height, V = tsunami speed, c = speed of sound) that serves as a filter to TAGWs in the atmosphere.

The intensification of thermo-viscous dissipation at thermospheric heights filters small-scale TAGWs, along with tilting of phase fronts vertically, as they shift to higher intrinsic frequencies (Hines, 1968; Vadas, 2007). Leading phases of the TAGW packet and thermospherically generated SAGWs may drive earlier-than-tsunami arrival perturbations, which is consistent with previous finding (Bagiya et al., 2017; Vadas et al., 2015). For example, the coherent structure of TEC perturbations and ionospheric airglow that are detected ahead of the tsunami over the Hawaiian Islands by Makela et al. (2011) ($\lambda_x = 290 \pm 12.5$ km, $v_x = 184.5 \pm 33.8$ m/s, and $\lambda_x = 189.9 \pm 4.9$ km, $v_x = 222.9 \pm 52.4$ m/s) points to leading phases as their source, whereas SAGWs propagate with much faster v_x.

Nonlinear evolution of TAGWs, generated by large tsunamis along a main lobe of tsunami energy, can lead to substantially different dynamics in comparison with linear assumptions. Self-acceleration effects cause the distortion of TAGW phases, which are followed by instabilities. In addition to recent modeling results on self-acceleration effects and instabilities in the lower thermosphere and below (Dong et al., 2020; Fritts & Lund, 2011), our results suggest they can develop in the lower regions of the F-layer of the ionosphere.

TAGW instabilities lead to the generation of acoustic and gravity waves, spanning broad range of periods, many that are radiated downward to form ducted waves that persist after the TAGWs' passage.

Undersea seamounts and plateaus, rises and escarpments cause reflection, refraction, and trapping of ocean surface waves, as well as their acceleration or slowdown. We demonstrated that these dynamics may also markedly affect TAGW characteristics and amplitudes. Thus, highly varying bathymetry in the West Pacific Ocean (Shatsky and Hess rises, HESC, MPM, IBMA, etc.) drastically affects TAGW characteristics. This also seems to be true for the Indian Ocean, where marked undersea features (e.g., Ninetyeast Ridge and Diamantina Fracture Zone) can result in a substantial variability of tsunamis and subsequent TAGWs. Focusing and branching of tsunami waves cause their amplification up to an order in magnitude (Berry, 2007; Degueldre et al., 2016) and TAGWs can experience marked variations of amplitudes. Bathymetry variations may also lead to the superposition of TAGW phases inside the packet. Below the thermosphere, TAGW mimic the tsunami wave evolution, exhibiting the same amplitude variations. At ionospheric altitudes, only large undersea scale massifs (such as the Shatsky Rise) result in notable change of TAGW characteristics. Finally, TAGWs may propagate inland and still drive comparable perturbations even ~1,000–1,500 km away from the shore, filtering toward larger dominant λ_x. These outcomes are also supported by previous observational studies, for example, by Azeem et al. (2017), finding traveling ionospheric disturbances driven by the Tohoku-Oki tsunami based on TEC observations as far inland as western Colorado, while λ_x of TEC disturbances increased from ~150–250 to ~250–400 km with distance.

In Figure 1i, we depict background temperature profile that was incorporated to the simulation of TAGWs in the Tohoku-Oki case study. At thermospheric heights, the temperature reaches almost 1,200 K. In addition to the fact that Tohoku-Oki tsunami was one of the largest recent tsunamis, "hot" thermospheric state results in large simulated perturbations along main energy lobe of the tsunami to the east and southeast. It is feasible that tsunami heights can be retrieved from upper atmosphere observations and can be useful for future applications and tsunami early-warning systems (Rakoto et al., 2018; Savastano et al., 2017). Recent efforts are also directed toward the development of systems for real-time detection of TAGWs based on TEC perturbations with both ground- and space-based observations (Savastano & Ravanelli, 2020). However, it is not yet clear how accurately the ocean response can be retrieved while incorporating nonlinearity in the atmosphere and bathymetry effects in the ocean. The detailed comparisons of models and data, as well as experiments with synthetic data, are needed. Thus, further studies can be directed toward the investigation of mesopause and ionospheric airglow signatures, as well as ionospheric plasma responses to TAGWs and characteristics of detected signals with an incorporation of realistic bathymetry and ITDs. Studies may also address the dispersive nature of tsunamis and full 3D ocean-atmosphere coupling, that will provide deep insight into atmosphere responses to undersea earthquakes and tsunamis generated by them.

Data Availability Statement

Finite-fault model for forward seismic wave propagation simulation was taken online (https://ji.faculty. geol.ucsb.edu/big_earthquakes/2011/03/0311_v3/Honshu.html). For tsunami simulation, we used 500 m Gridded Bathymetry Data (J-EGG500) (https://www.jodc.go.jp/jodcweb/JDOSS/infoJEGG.html) with USGS GTOPO30 land portion (www.jodc.go.jp/jodcweb/JDOSS) near the Japan Islands area and 1-min resolution ETOPO1 bathymetry by NOAA (https://www.ngdc.noaa.gov/mgg/topo/topo.html). Tsunami simulation codes can be found online (https://www.clawpack.org/geoclaw.html). Supplementary materials and data can be found online (https://commons.erau.edu/dm-tsunamigenic-acoustic-gravity-waves/).

References

Artru, J., Ducic, V., Kanamori, H., Lognonné, P., & Murakami, M. (2005). Ionospheric detection of gravity waves induced by tsunamis. *Geophysical Journal International*, *160*(3), 840–848. https://doi.org/10.1111/j.1365-246X.2005.02552.x

Azeem, I., Vadas, S. L., Crowley, G., & Makela, J. J. (2017). Traveling ionospheric disturbances over the United States induced by gravity waves from the 2011 Tohoku tsunami and comparison with gravity wave dissipative theory. *Journal of Geophysical Research: Space Physics*, *122*, 3430–3447. https://doi.org/10.1002/2016JA023659

Bagiya, M. S., Kherani, E. A., Sunil, P. S., Sunil, A. S., Sunda, S., & Ramesh, D. S. (2017). Origin of the ahead of tsunami traveling ionospheric disturbances during Sumatra tsunami and offshore forecasting. *Journal of Geophysical Research: Space Physics*, *122*, 7742–7749. https://doi.org/10.1002/2017JA023971

Berger, M. J., George, D. L., LeVeque, R. J., & Mandli, K. T. (2011). The GeoClaw software for depth-averaged flows with adaptive refinement. *Advances in Water Resources*, *34*, 1195–1206.

Berry, M. V. (2007). Focused tsunami waves. *Proceedings of the Royal Society A: Mathematical, Physical and Engineering Sciences*, *463*(2087), 3055–3071. https://doi.org/10.1098/rspa.2007.0051

Bossert, K., Kruse, C. G., Heale, C. J., Fritts, D. C., Williams, B. P., Snively, J. B., et al. (2017). Secondary gravity wave generation over New Zealand during the DEEPWAVE campaign. *Journal of Geophysical Research: Atmospheres*, *122*, 7834–7850. https://doi.org/10.1002/2016JD026079

Broutman, D., Eckermann, S. D., & Drob, D. P. (2014). The partial reflection of tsunami-generated gravity waves. *Journal of the Atmospheric Sciences*, *71*(9), 3416–3426. https://doi.org/10.1175/JAS-D-13-0309.1

Chimonas, G., & Hines, C. O. (1986). Doppler ducting atmospheric gravity waves. *Journal of Geophysical Research*, *91*(D1), 1219–1230. https://doi.org/10.1029/JD091iD01p01219

Clawpack Development Team (2018). Clawpack software. Retrieved from http://www.clawpack.org (Version 5.5.0) https://doi.org/10.5281/zenodo.1405834

Coïsson, P., Lognonnè, P., Walwer, D., & Rolland, L. M. (2015). First tsunami gravity wave detection in ionospheric radio occultation data. *Earth and Space Science*, *2*, 125–133. https://doi.org/10.1002/2014EA000054

Davies, K., & Baker, D. M. (1965). Ionospheric effects observed around the time of the Alaskan earthquake of March 28, 1964. *Journal of Geophysical Research*, *70*(9), 2251–2253.

Degueldre, H., Metzger, J. J., Geisel, T., & Fleischmann, R. (2016). Random focusing of tsunami waves. *Nature Physics*, *12*(3), 1745–2481. https://doi.org/10.1038/nphys3557

Dong, W., Fritts, D. C., Lund, T. S., Wieland, S. A., & Zhang, S. (2020). Self-Acceleration and instability of gravity wave packets: 2. Two-dimensional packet propagation, instability dynamics, and transient flow responses. *Journal of Geophysical Research: Atmospheres*, *125*, e2019JD030691. https://doi.org/10.1029/2019JD030691

Drob, D. P., Emmert, J. T., Meriwether, J. W., Makela, J. J., Doornbos, E., Conde, M., et al. (2015). An update to the horizontal wind model (HWM): The quiet time thermosphere. *Earth and Space Science*, *2*(7), 301–319. https://doi.org/10.1002/2014EA000089

Fritts, D. C., Laughman, B., Lund, T. S., & Snively, J. B. (2015). Self-acceleration and instability of gravity wave packets: 1. Effects of temporal localization. *Journal of Geophysical Research: Atmospheres*, *120*, 8783–8803. https://doi.org/10.1002/2015JD023363

Fritts, D. C., & Lund, T. S. (2011). Gravity wave influences in the thermosphere and ionosphere: Observations and recent modeling. In M. A. Abdu, & D. Pancheva (Eds.), *Aeronomy of the Earth's Atmosphere and Ionosphere* (pp. 109–130). Dordrecht: Springer Netherlands. https://doi.org/10.1007/978-94-007-0326-1_8

Fritz, H. M., Phillips, D. A., Okayasu, A., Shimozono, T., Liu, H., Mohammed, F., et al. (2012). The 2011 Japan tsunami current velocity measurements from survivor videos at Kesennuma Bay using LiDAR. *Geophysical Research Letters*, *39*, L00G23. https://doi.org/10.1029/2011GL050686

Galvan, D. A., Komjathy, A., Hickey, M. P., & Mannucci, A. J. (2011). The 2009 Samoa and 2010 Chile tsunamis as observed in the ionosphere using GPS total electron content. *Journal of Geophysical Research*, *116*, A06318. https://doi.org/10.1029/2010JA016204

Galvan, D. A., Komjathy, A., Hickey, M. P., Stephens, P., Snively, J., Tony Song, Y., et al. (2012). Ionospheric signatures of Tohoku-Oki tsunami of March 11, 2011: Model comparisons near the epicenter. *Radio Science*, *47*(4), RS4003. https://doi.org/10.1029/2012RS005023

Godin, O. A., Zabotin, N. A., & Bullett, T. W. (2015). Acoustic-gravity waves in the atmosphere generated by infragravity waves in the ocean. *Earth, Planets and Space*, *67*(1), 47. https://doi.org/10.1186/s40623-015-0212-4

Gonzalez, F. I., LeVeque, R. J., Chamberlain, P., Hirai, B., Varkovitzky, J., & George, D. L. (2011). Validation of the GeoClaw model.

Hao, Y. Q., Xiao, Z., & Zhang, D. H. (2013). Teleseismic magnetic effects (TMDs) of 2011 Tohoku earthquake. *Journal of Geophysical Research: Space Physics*, *118*, 3914–3923. https://doi.org/10.1002/jgra.50326

Heale, C. J., Bossert, K., Vadas, S. L., Hoffmann, L., Dörnbrack, A., Stober, G., et al. (2020). Secondary gravity waves generated by breaking mountain waves over Europe. *Journal of Geophysical Research: Atmospheres*, *125*, e2019JD031662. https://doi.org/10.1029/2019JD031662

Heale, C. J., & Snively, J. B. (2015). Gravity wave propagation through a vertically and horizontally inhomogeneous background wind. *Journal of Geophysical Research: Atmospheres*, *120*, 5931–5950. https://doi.org/10.1002/2015JD023505

Heale, C. J., Snively, J. B., Hickey, M. P., & Ali, C. J. (2014). Thermospheric dissipation of upward propagating gravity wave packets. *Journal of Geophysical Research: Space Physics*, *119*, 3857–3872. https://doi.org/10.1002/2013JA019387

Hickey, M. P., Schubert, G., & Walterscheid, R. L. (2009). Propagation of tsunami-driven gravity waves into the thermosphere and ionosphere. *Journal of Geophysical Research*, *114*, A08304. https://doi.org/10.1029/2009JA014105

Hines, C. O. (1968). An effect of molecular dissipation in upper atmospheric gravity waves. *Journal of Atmospheric and Terrestrial Physics*, *30*(5), 845–849. https://doi.org/10.1016/S0021-9169(68)80036-4

Huba, J. D., Drob, D. P., Wu, T.-W., & Makela, J. J. (2015). Modeling the ionospheric impact of tsunami-driven gravity waves with SAMI3: Conjugate effects. *Geophysical Research Letters*, *42*, 5719–5726. https://doi.org/10.1002/2015GL064871

Inchin, P. A., Snively, J. B., Williamson, A., Melgar, D., Aguilar Guerrero, J., & Zettergren, M. D. (2020). Mesopause airglow disturbances driven by nonlinear infrasonic acoustic waves generated by large earthquakes. *Journal of Geophysical Research: Space Physics*, *125*, e2019JA027628. https://doi.org/10.1029/2019JA027628

Kamogawa, M., Orihara, Y., Tsurudome, C., Tomida, Y., Kanaya, T., Ikeda, D., et al. (2016). A possible space-based tsunami early warning system using observations of the tsunami ionospheric hole. *Nature Scientific Report*, *6*(37989). https://doi.org/10.1038/srep37989

Kherani, E. A., Rolland, L., Lognonné, P., Sladen, A., Klausner, V., & de Paula, E. R. (2015). Traveling ionospheric disturbances propagating ahead of the Tohoku-Oki tsunami: A case study. *Geophysical Journal International*, *204*(2), 1148–1158. https://doi.org/10.1093/gji/ggv500

Laughman, B., Fritts, D. C., & Lund, T. S. (2017). Tsunami-driven gravity waves in the presence of vertically varying background and tidal wind structures. *Journal of Geophysical Research: Atmospheres*, *122*, 5076–5096. https://doi.org/10.1002/2016JD025673

Lay, T. (2018). A review of the rupture characteristics of the 2011 Tohoku-Oki Mw 9.1 earthquake. *Tectonophysics*, *733*, 4–36. https://doi.org/10.1016/j.tecto.2017.09.022

Levin, B., & Nosov, M. (2016). *Physics of tsunamis*. Switzerland: Springer International Publishing. https://doi.org/10.1007/978-3-319-24037-4

Liu, J.-Y., Chen, C.-H., Lin, C.-H., Tsai, H.-F., Chen, C.-H., & Kamogawa, M. (2011). Ionospheric disturbances triggered by the 11 March 2011 M9.0 Tohoku earthquake. *Journal of Geophysical Research*, *116*, A06319. https://doi.org/10.1029/2011JA016761

MacInnes, B. T., Gusman, A. R., LeVeque, R. J., & Tanioka, Y. (2013). Comparison of earthquake source models for the 2011 Tohoku event using tsunami simulations and near-field observations. *Bulletin of the Seismological Society of America*, *103*(2B), 1256. https://doi.org/10.1785/0120120121

Makela, J. J., Lognonné, P., Hébert, H., Gehrels, T., Rolland, L., Allgeyer, S., et al. (2011). Imaging and modeling the ionospheric airglow response over hawaii to the tsunami generated by the Tohoku earthquake of 11 March 2011. *Geophysical Research Letters*, *38*, L00G02. https://doi.org/10.1029/2011GL047860

Maruyama, T., & Shinagawa, H. (2014). Infrasonic sounds excited by seismic waves of the 2011 Tohoku-Oki earthquake as visualized in ionograms. *Journal of Geophysical Research: Space Physics*, *119*, 4094–4108. https://doi.org/10.1002/2013JA019707

Mofjeld, H. O. (2000). Analytic theory of tsunami wave scattering in the open ocean with application to the North Pacific.

Mori, N., Takahashi, T., Yasuda, T., & Yanagisawa, H. (2011). Survey of 2011 Tohoku earthquake tsunami inundation and run-up. *Geophysical Research Letters*, *38*, L00G14. https://doi.org/10.1029/2011GL049210

Nappo, C. J. (2013). *An introduction to atmospheric gravity waves*: Academic press.

Occhipinti, G., Rolland, L., Lognonné, P., & Watada, S. (2013). From Sumatra 2004 to Tohoku-Oki 2011: The systematic GPS detection of the ionospheric signature induced by tsunamigenic earthquakes. *Journal of Geophysical Research: Space Physics*, *118*, 3626–3636. https://doi.org/10.1002/jgra.50322

Peltier, W. R., & Hines, C. O. (1976). On the possible detection of tsunamis by a monitoring of the ionosphere. *Journal of Geophysical Research*, *81*(12), 1995–2000. https://doi.org/10.1029/JC081i012p01995

Picone, J. M., Hedin, A. E., Drob, D. P., & Aikin, A. C. (2002). NRLMSISE-00 empirical model of the atmosphere: Statistical comparisons and scientific issues. *Journal of Geophysical Research*, *107*(A12), SIA 15–1–SIA 15–16. https://doi.org/10.1029/2002JA009430

Rakoto, V., Lognonné, P., Rolland, L., & Coïsson, P. (2018). Tsunami wave height estimation from GPS-derived ionospheric data. *Journal of Geophysical Research: Space Physics*, *123*, 4329–4348. https://doi.org/10.1002/2017JA024654

Saito, A., Tsugawa, T., Otsuka, Y., Nishioka, M., Iyemori, T., Matsumura, M., et al. (2011). Acoustic resonance and plasma depletion detected by GPS total electron content observation after the 2011 off the Pacific coast of Tohoku earthquake. *Earth, Planets and Space*, *63*(7), 64.

Satake, K. (1988). Effects of bathymetry on tsunami propagation: Application of ray tracing to tsunamis. *PAGEOPH*, *126*, 27–36. https://doi.org/10.1007/BF00876912

Savastano, G., Komjathy, A., Verkhoglyadova, O., Mazzoni, A., Crespi, M., Wei, Y., & Mannucci, A. J. (2017). Real-time detection of tsunami ionospheric disturbances with a stand-alone GNSS receiver: A preliminary feasibility demonstration. *Nature*, *7*, 46,607.

Savastano, G., & Ravanelli, M. (2020). Real-time monitoring of ionospheric irregularities and TEC perturbations, *Satellites Missions and Technologies for Geosciences*. Rijeka: IntechOpen. https://doi.org/10.5772/intechopen.90036

Shao, G., Li, X., Ji, C., & Maeda, T. (2011). Focal mechanism and slip history of the 2011 Mw 9.1 off the Pacific coast of Tohoku earthquake, constrained with teleseismic body and surface waves. *Earth, Planets and Space*, *63*(7), 559–564. https://doi.org/10.5047/eps.2011.06.028

Snively, J. B. (2013). Mesospheric hydroxyl airglow signatures of acoustic and gravity waves generated by transient tropospheric forcing. *Geophysical Research Letters*, *40*, 4533–4537. https://doi.org/10.1002/grl.50886

Snively, J. B. (2017). Nonlinear gravity wave forcing as a source of acoustic waves in the mesosphere, thermosphere, and ionosphere. *Geophysical Research Letters*, *44*, 12,020–12,027. https://doi.org/10.1002/2017GL075360

Snively, J. B., & Pasko, V. P. (2008). Excitation of ducted gravity waves in the lower thermosphere by tropospheric sources. *Journal of Geophysical Research*, *113*, A06303. https://doi.org/10.1029/2007JA012693

Sutherland, B. R. (2006). Internal wave instability: Wave-wave versus wave-induced mean flow interactions. *Physics of Fluids*, *18*(7), 74,107. https://doi.org/10.1063/1.2219102

Sutherland, B. R., & Yewchuk, K. (2004). Internal wave tunnelling. *Journal of Fluid Mechanics*, *511*, 125–134. https://doi.org/10.1017/S0022112004009863

Tang, L., Zhao, Y., & An, J. (2016). First GPS TEC maps of ionospheric disturbances induced by reflected tsunami waves: The Tohoku case study. *Natural Hazards and Earth System Sciences Discussions*, *2016*, 1–14. https://doi.org/10.5194/nhess-2016-11

Tsugawa, T., Saito, A., Otsuka, Y., Nishioka, M., Maruyama, T., Kato, H., et al. (2011). Ionospheric disturbances detected by GPS total electron content observation after the 2011 off the pacific coast of Tohoku earthquake. *Earth, Planets and Space*, *63*(7), 66. https://doi.org/10.5047/eps.2011.06.035

Vadas, S. L. (2007). Horizontal and vertical propagation and dissipation of gravity waves in the thermosphere from lower atmospheric and thermospheric sources. *Journal of Geophysical Research*, *112*, A06305. https://doi.org/10.1029/2006JA011845

Vadas, S. L., Makela, J. J., Nicolls, M. J., & Milliff, R. F. (2015). Excitation of gravity waves by ocean surface wave packets: Upward propagation and reconstruction of the thermospheric gravity wave field. *Journal of Geophysical Research: Space Physics*, *120*, 9748–9780. https://doi.org/10.1002/2015JA021430

Walterscheid, R. L., & Schubert, G. (1990). Nonlinear evolution of an upward propagating gravity wave: Overturning, convection, transience and turbulence. *Journal of the Atmospheric Sciences*, *47*(1), 101–125. https://doi.org/10.1175/1520-0469(1990)047<0101:NEOAUP>2.0.CO;2

Wei, C., Bühler, O., & Tabak, E. G. (2015). Evolution of tsunami-induced internal acoustic-gravity waves. *Journal of the Atmospheric Sciences*, *72*(6), 2303–2317. https://doi.org/10.1175/JAS-D-14-0179.1

Wu, Y., Llewellyn Smith, S. G., Rottman, J. W., Broutman, D., & Minster, J.-B. H. (2016). The propagation of tsunami-generated acoustic-gravity waves in the atmosphere. *Journal of the Atmospheric Sciences*, *73*(8), 3025–3036. https://doi.org/10.1175/JAS-D-15-0255.1

Wu, Y., Llewellyn Smith, S. G., Rottman, J. W., Broutman, D., & Minster, J.-B. H. (2020). Time-dependent propagation of tsunami-generated acoustic-gravity waves in the atmosphere. *Journal of the Atmospheric Sciences*, *77*(4), 1233–1244. https://doi.org/10.1175/JAS-D-18-0322.1

Yang, Y.-M., Meng, X., Komjathy, A., Verkholyadova, O., Langley, R. B., Tsurutani, B. T., & Mannucci, A. J. (2014). Tohoku-Oki earthquake caused major ionospheric disturbances at 450 km altitude over Alaska. *Radio Science*, *49*(12), 1206–1213. https://doi.org/10.1002/2014RS005580

Yang, Y.-M., Verkhoglyadova, O., Mlynczak, M. G., Mannucci, A. J., Meng, X., Langley, R. B., & Hunt, L. A. (2017). Satellite-based observations of tsunami-induced mesosphere airglow perturbations. *Geophysical Research Letters*, *44*, 522–532. https://doi.org/10.1002/2016GL070764

Yu, Y., & Hickey, M. P. (2007). Numerical modeling of a gravity wave packet ducted by the thermal structure of the atmosphere. *Journal of Geophysical Research*, *112*, A06308. https://doi.org/10.1029/2006JA012092